Efficient simulation of railway pantograph/ catenary interaction using pantograph-fixed coordinates

Daniel Ritzberger * **Emir Talic** * **Alexander Schirrer** *

* *Vienna University of Technology, Austria, (e-mail: daniel.ritzberger@gmail.com).*

Abstract: In this paper, a novel approach for the simulation of the railway catenary and pantograph dynamics is proposed. The partial differential equations describing the vertical motion of the contact and carrier wires of the catenary are transformed in such a way that the pantograph is at rest with respect to the new moving coordinate. The computational domain is then truncated and absorbing boundary conditions are applied. High computational performance due to a great reduction in variables is achieved. The differences between this small scale system and a reference system with a fixed catenary length and a moving pantograph are investigated.

Keywords: Modelling Aspects in Scientific Computing; Numerical and Symbolical Methods for Modelling

1. INTRODUCTION

A numerical simulation of the complex catenary and pantograph dynamics (see Fig. 1) can give a better insight on how they interact with one another and lead to better design rules for the pantograph to prevent contact loss and electric arcing. The dynamics are described by coupled partial differential equations (PDEs). The classic approach for modelling the pantograph and catenary interaction, see Arnold and Simeon (2000) and Poetsch et al. (1997), is with respect to a resting catenary and a moving pantograph. This formulation is also predominant in many recent papers studying more complex phenomena like wind disturbances and co-simulation of multi-body pantograph models, see Pombo et al. (2009). For real-time applications a simplified mathematical model of the catenary can be obtained by using the modal superposition principle (Facchinetti and Bruni (2012), Zhang et al. (2002)). In the resting catenary formulation, the maximal simulation time is limited by the length of the catenary. Longer simulations consequently increase the number of variables of the dynamical system and the computational effort. Also if the pantograph is currently moving near the boundary, reflections occur. These unphysical reflections decrease the quality of the simulation and directly disturb the pantograph-catenary-interaction. A new approach that deals with these problems is presented here.

In this work a new formulation for the problem is introduced with the goal to make the size of the computational domain independent from the simulation time, and reducing the computational effort, so that the simulation can be carried out in real-time. This is achieved by a transformation of the PDEs, which describe the catenary dynamics, to moving coordinates. The pantograph is now at a fixed location with respect to the new coordinate and the catenary moves over the pantograph through the computational domain. To eliminate the disturbances due to reflections at the boundaries, absorbing boundary conditions (ABCs) are introduced which ideally let waves leave the computational domain without reflections. Thus, the length of this system can be chosen reasonably small, reducing the number of variables to be calculated. Using the transformed equations with a fixed pantograph an "endless" catenary is approximated on a bounded computational domain.

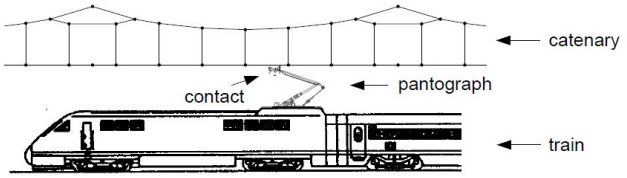

Fig. 1. System Catenary/ Pantograph, taken from Poetsch et al. (1997)

The structure of this paper is as follows: In chapter 2, the methodology used for the novel system formulation is discussed. In chapter 3, a concrete numerical system is assembled, and in chapter 4, the small-scale moving system and a large reference system with fixed catenary and moving pantograph are compared in numerical results.

2. METHODOLOGY

In this chapter, the equation of motion for a pretensioned Euler-Bernoulli-Beam equation, its transformation to a moving coordinate, a simple ABC formulation and its discretization are discussed.

2.1 Transforming the Equations of Motion

The transversal motion of the contact and carrier wire is described by a pretensioned Euler-Bernoulli-Beam equation.

$$\rho A\frac{\partial^2 w(x,t)}{\partial t^2}+\beta\frac{\partial w(x,t)}{\partial t}=-EI\frac{\partial^4 w(x,t)}{\partial x^4}+T\frac{\partial^2 w(x,t)}{\partial x^2}+f(x,t) \tag{1}$$

Thereby, ρA is the mass per unit length, β the damping constant, EI the bending stiffness, T the tensile axial force and $f(x,t)$ is the vertical force density. Equation (1) is transformed using a new coordinate $\hat{x}(t)=x+vt$ where v is the constant pantograph speed. Because $\frac{\partial\hat{x}}{\partial x}=1$, the spatial partial derivatives, $\frac{\partial^n w(x(t),t)}{\partial x^n}=\frac{\partial^n w(\hat{x}(t),t)}{\partial \hat{x}^n}$, remains simple. The new coordinate is time-dependent, which has to be considered for the partial derivative with respect to t. Using implicit differentiation one obtains

$$\frac{dw(\hat{x}(t),t)}{dt}=\frac{\partial w(\hat{x},t)}{\partial t}-v\frac{\partial w(\hat{x},t)}{\partial \hat{x}} \tag{2}$$

and

$$\frac{d^2 w(\hat{x}(t),t)}{dt^2}=\frac{\partial^2 w(\hat{x},t)}{\partial t^2}-2v\frac{\partial^2 w(\hat{x},t)}{\partial \hat{x}\partial t}+v^2\frac{\partial^2 w(\hat{x},t)}{\partial \hat{x}^2} \tag{3}$$

Inserting (2) and (3) into (1) leads to the following equation of motion for a pretensioned Euler-Bernoulli beam with respect to a moving spatial coordinate.

$$\rho A\ddot{w}+\beta\dot{w}=-EIw''''+(T-\rho Av^2)w''+\beta vw'+2v\rho A\dot{w}'+f(\hat{x},t) \tag{4}$$

To keep the notation simple the abbreviations $\frac{\partial w}{\partial t}=\dot{w}$ and $\frac{\partial w}{\partial \hat{x}}=w'$ are used, with higher order of derivatives respectively. Note that the transformed equation of motion now contains the mixed derivative $\dot{w}'$.

2.2 Absorbing Boundary Conditions

ABCs are used to minimize the reflections of waves at the computational boundary. For a detailed discussion of the ABCs see Engquist and Majda (1977) or Higdon (1987). The first order approximation of the perfect absorbing boundary condition is used, which is exact for the one-dimensional wave equation:

$$\dot{w}\pm(c\mp v)w'=0,\qquad c=\sqrt{\frac{T}{\rho A}}, \tag{5}$$

where c is the wave speed. Eq. (5) has to be fulfilled at the boundary. The signs of the second term differs for the left and for the right boundary, as there are left- and right-going waves to be absorbed, and the wave speed for left going waves is increased by v while the wave speed for right going waves is decreased by v.

A stable discretization of Eq. (5) is obtained by using a forward difference approximation for the partial derivative with respect to time. The spatial partial derivative is discretized by forward differences for the left boundary and backward differences for the right boundary. This leads to the discrete ABC for the left boundary

$$w_1^{j+1}=(1-(c+v)\frac{\Delta t}{\Delta x})w_1^j+(c+v)\frac{\Delta t}{\Delta x}w_2^j \tag{6}$$

and for the right boundary

$$w_{n_{max}}^{j+1}=(1-(c-v)\frac{\Delta t}{\Delta x})w_{n_{max}}^j+(c-v)\frac{\Delta t}{\Delta x}w_{n_{max}-1}^j \tag{7}$$

The discrete ABCs are only exact for the scalar wave equation and if

$$\frac{\Delta t}{\Delta x}=\frac{1}{c} \tag{8}$$

Since Eq. (6) and (7) are imposed on the pretensioned Euler-Bernoulli-beam and the ratio for the spatial and temporal grid size (8) cannot be set to c because of stability issues, the ABCs are not exact and reflections occur. Using the scalar wave ABCs is the first approach on introducing reflectionless boundaries for the pretensioned Euler-Bernoulli beam. In future work, a genetically optimized boundary stencil for the moving Euler-Bernoulli beam will be used, see Schirrer et al. (2014)

3. SYSTEM ASSEMBLY

Using the methodology discussed above, a dynamic formulation of the catenary/ pantograph interaction and its discretization is obtained.

3.1 Description

As it can be seen in Fig. 2, the catenary consists of two wires, the carrier and the contact wire. The contact wire is suspended by droppers from the carrier wire in such a way that the static displacement of the contact wire is minimized. The head of the pantograph pushes against the contact wire.

For the contact and the carrier wire, the transformed Euler-Bernoulli beam equation (4)

$$\rho_c A_c\ddot{w}_c+\beta_c\dot{w}_c=-E_cI_cw_c''''+(T_c-\rho_cA_cv^2)w_c''+\beta_cvw_c'+2\rho_cA_cv\dot{w}_c'+f_c(\hat{x},t) \tag{9}$$

$$\rho_w A_w\ddot{w}_w+\beta_w\dot{w}_w=-E_wI_ww_w''''+(T_w-\rho_wA_wv^2)w_w''+\beta_wvw_w'+2\rho_wA_wv\dot{w}_w'+f_w(\hat{x},t) \tag{10}$$

is used.

The subscript w denotes the displacement and parameters for the contact wire and c the displacement and parameters for the carrier wire.
The pantograph is modelled as a two-mass oscillator. Its equations of motion are given by

$$\begin{aligned}m_1w_{p,1}&=-d_1(\dot{w}_{p,1}-\dot{w}_{p,2})-c_1(w_{p,1}-w_{p,2})-F_{cont}\\ m_2w_{p,2}&=-d_2\dot{w}_{p,2}+d_1(\dot{w}_{p,1}-\dot{w}_{p,2})-c_2w_{p,2}+\\&\quad c_1(w_{p,1}-w_{p,2})+F_0\end{aligned} \tag{11}$$

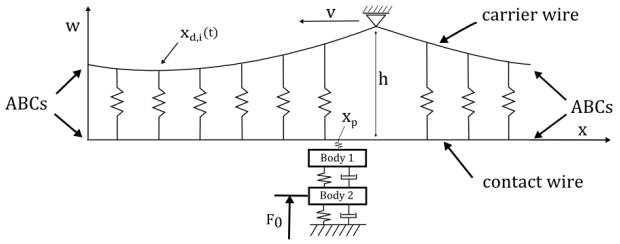

Fig. 2. Catenary and Pantograph system description

where m_n is the mass of body n. c_1 and d_1 are the spring and damping coefficients between the two masses and c_2 and d_2 the spring and damping between the second mass and the inertial reference frame. F_{cont} is the contact force between the first mass and the contact wire and F_0 is a static force. The contact force is given by

$$\begin{aligned} F_{cont} &= k_{cont}(w_{p,1} - w_w(x_p)) \quad if \quad w_{p,1} - w_w(x_p) > 0 \\ F_{cont} &= 0 \qquad\qquad\qquad\qquad\quad if \quad w_{p,1} - w_w(x_p) \leq 0 \end{aligned} \tag{12}$$

The droppers between the contact and the carrier wire are modelled as a spring, so that the force of the dropper i acting on the contact and carrier wire can be evaluated by

$$F_{d,i} = k_{d,i}[w_c(x_{d,i}(t)) - w_w(x_{d,i}(t)) - l_{0,i}] \tag{13}$$

Here, $x_{d,i}$ denotes the position of the dropper i which changes in time due to the catenary movement, and $l_{0,i}$ is the unstretched length of the dropper.

3.2 Discretizing the equations of motion

To ensure fast numerical solving, a simple finite difference discretization method was chosen. For a detailed discussion on finite difference methods see Gustafsson et al. (2013). The spatial and temporal partial differentiations are substituted with the corresponding central difference schemes, e.g.

$$\ddot{w}(x,t) = \frac{w_n^{j+1} - 2w_n^j + w_n^{j-1}}{\Delta t^2} \tag{14}$$

and

$$w''(x,t) = \frac{w_{n+1}^j - 2w_n^j + w_{n-1}^j}{\Delta x^2} \tag{15}$$

Discretizing the equations of motion (9)–(11) leads to a state-space system of the form

$$\mathbf{A}\underline{q}^{j+1} = \mathbf{B}\underline{q}^j + \mathbf{C}\underline{q}^{j-1} + \mathbf{f}^j(t) \tag{16}$$

The vector of coordinates $\underline{q}^j$ was chosen as

$$\underline{q}^j = [w_{c_1}^j \dots w_{c_n}^j, w_{w_1}^j \dots w_{w_n}^j, w_{p,1}^j, w_{p,2}^j]. \tag{17}$$

By inverting the matrix $\mathbf{A}$, the vector for the next time step, depending on the vector of the current and the last time steps, can be computed.
The transformation to the new coordinate leads to the mixed derivative term in (4). If this term is discretized using central differences, the matrix $\mathbf{A}$ is tridiagonal, and inverting $\mathbf{A}$ on $\mathbf{B}$ and $\mathbf{C}$ leads to block-wise fully populated matrices, which increases the computational effort. On the other hand, if the mixed derivative term is discretized by a backwards difference approximation for the partial derivative with respect to time, the matrix $\mathbf{A}$ remains diagonal, and inverting it does not change the sparse structure of the matrices and therefore does not increase the computational effort for each step. However, the backwards difference approximation drastically reduces the maximum stable time step size compared to the central difference approximation. Hence, for the same simulation time, more steps have to be computed. The central difference approximation was chosen because the benefit of a larger stable time step size outweighs the sparsity of the system matrices in terms of computational effort.

3.3 Decoupling of the static and dynamic computation

In (16) the force density vector $\mathbf{f}(t)$ contains static components, such as the static force density due to gravitation on each discretization point

$$f_{c/w}^j = -\rho_{c/w} A_{c/w} g \tag{18}$$

where g is the gravitational constant, or the static component of the dropper force due to the unstretched length. With Dirichlet boundary conditions, those constant forces result in a constant displacement of the catenary. This is not the case when absorbing boundary conditions are introduced. A constant force with ABCs imposed leads to a continuously increasing displacement of the catenary. In chapter 4 the small-scale system formulation presented in this paper will be compared to a non-moving, large-scale, reference system which is described in Arnold and Simeon (2000). This large-scale reference system has a well-defined static solution because the global setup (and boundary conditions) can exert the corresponding restoring forces. Thus, in the large-scale reference system, the static and dynamic portions of the solution can be computed together, whereas to make the problem solvable on the small-scale system, equation (16) is split into the following two parts.

$$\mathbf{A}_{stat}\underline{q}_s^{j+1} = \mathbf{B}_{stat}\underline{q}_s^j + \mathbf{C}_{stat}\underline{q}_s^{j-1} + \mathbf{f}_{stat} \tag{19}$$

$$\mathbf{A}_{dyn}\underline{q}_d^{j+1} = \mathbf{B}_{dyn}\underline{q}_d^j + \mathbf{C}_{dyn}\underline{q}_d^{j-1} + \mathbf{f}_{dyn}(t) \tag{20}$$

In $\mathbf{f}_{stat}$ all the static forces are collected. The system matrices in Eq. (19) and (20) differ, because in (19) the ABCs are replaced with Dirichlet boundary conditions at mast position for the carrier wire, and periodic boundary conditions for the contact wire. For equation (19) a static solution $\underline{q}_{stat}^j$ can be found. The total solution is then given by

$$\underline{q}^j = \underline{q}_d^j + \underline{q}_{stat}^j \tag{21}$$

The static solution differs for every time step, since the mast and dropper position changes. However, one can use the periodic nature of the catenary to avoid recomputing Eq. (19) at every sampling instance:

$$q_{stat}^{j+1}(n\Delta x) = q_{stat}^j(n\Delta x + \Delta t v) \tag{22}$$

Since the q^j_{stat} is only known at discrete points, and $n\Delta x + \Delta t v$ lies generally between two grid points, quadratic interpolation is used to calculate the value of the static solution between two discrete points. Once k time steps have been computed so that

$$n\Delta x + k\Delta t v \geq (n+1)\Delta x, \tag{23}$$

one can shift the entire static solution

$$\underline{q}^{j+k}_{stat} = \begin{pmatrix} 0 & 1 & 0 & 0 & \dots \\ 0 & 0 & 1 & 0 & \dots \\ 0 & 0 & 0 & 1 & \dots \\ \vdots & & & & \ddots \\ 1 & 0 & 0 & 0 & \dots \end{pmatrix} \underline{q}^{j}_{stat} \tag{24}$$

The static solution is now only computed at the first time step, and for every following step it is obtained by shifting and interpolation.

3.4 Adjusting the dropper stiffness

The small scale system has no information of incoming droppers. When a dropper enters the domain, sudden large dropper forces disturb the solution as the ABCs let waves leave the computational domain freely and do not take into account that there is a certain restriction in the height difference of contact and carrier wire due to the dropper approaching the computational boundary. To smooth those disturbances, the stiffness of the dropper is adjusted with a blending function:

$$k_d(x_{bd}) = \frac{x_{bd}}{b} - \sin\left(\frac{2\pi x_{bd}}{b}\right)\frac{1}{2\pi} \tag{25}$$

x_{bd} denotes the distance between the dropper and the boundary it has entered and b is the width of the blending area after which the dropper stiffness is restored to its full value (see fig. 3). A satisfying reduction of high frequency distortions by the entering droppers is achieved by a blending area width of about 10-20% of the computational domain.

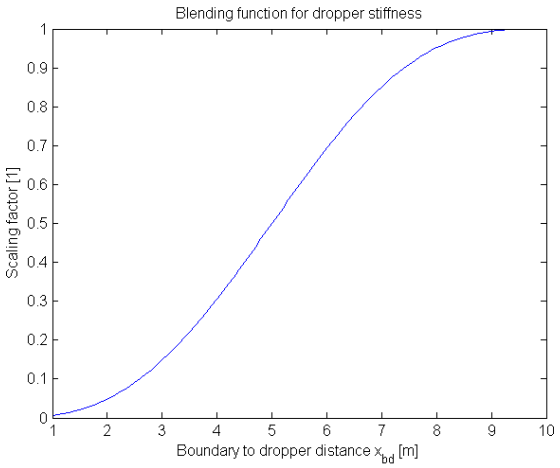

Fig. 3. Blending function for the dropper stiffness

4. SIMULATION RESULTS

The numerical results of two small-scale test cases are compared to its large scale, non-moving, reference system. At the end of this chapter, the computational times are compared.

4.1 Parameters

In the simulation, the parameters were set as outlined in Tables 1 and 2

Table 1. Catenary parameters

Parameter	Symbol	Value
length of span	l	60 [m]
distance carrier/contact wire	h	1.2 [m]
mass per unit length (carrier)	$\rho_c A_c$	1.07 [kg/m]
mass per unit length (contact)	$\rho_w A_w$	1.35 [km/m]
damping constant (carrier)	β_c	0.03 [Ns/m]
damping constant (contact)	β_w	0.03 [Ns/m]
bending stiffness (carrier)	$E_c I_c$	0 Nm^2
bending stiffness (contact)	$E_w I_w$	150 Nm^2
tensile force (carrier)	T_c	16 [kN]
tensile force (contact)	T_w	20 [kN]
gravitational constant	g	9.81 [m/s^2]
dropper stiffness	k_d	100 [kN/m]

Table 2. Pantograph parameters

Parameter	Symbol	Value
contact unilateral spring constant	k_{cont}	50 [kN/m]
spring constant 1	c_1	50 [N/m]
spring constant 2	c_2	4200 [N/m]
damping constant 1	d_1	90 [Ns/m]
damping constant 2	d_2	10 [Ns/m]
mass body 1	m_1	15 [kg]
mass body 2	m_2	7.2 [kg]
velocity	v	250 [km/h]

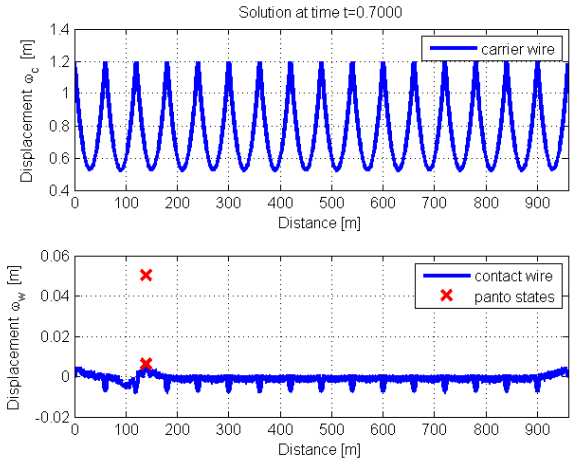

Fig. 4. Static Reference System

4.2 Test case 1: low constant force F_0

In Fig. 4 the large scale (LS) reference system is shown. At mast position, the distance between two subsequent

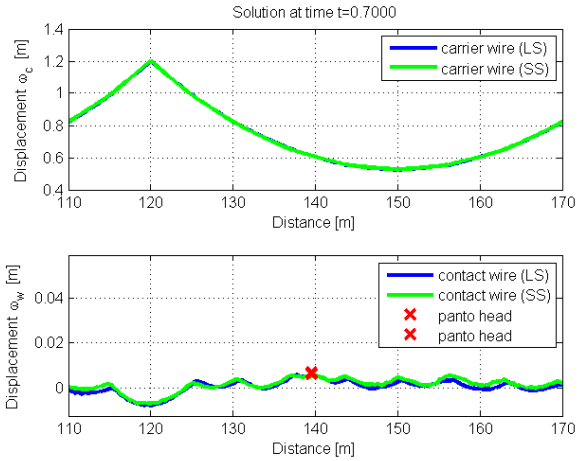

Fig. 5. Comparison between large scale (blue) and small scale (green) system with $F_0 = 260$ N. Node spacing Δx= 0.4 m

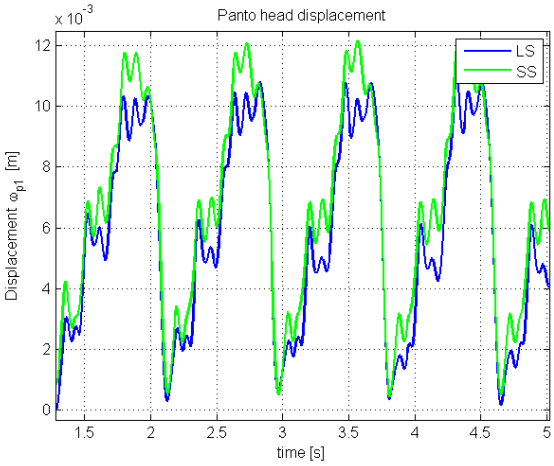

Fig. 6. Displacement over time for the pantograph head for the large scale (blue) and small scale (green) system with $F_0 = 260$ N

droppers was chosen to be twice as large. This results in negative peaks of the contact wire exciting the pantograph. The total length of the large scale reference system is 960 meters as there are 16 spans of 60 m each. The spatial grid size Δx was chosen to be 0.4 m. In sum, there are 4817 variables to be solved for the catenary. The temporal step size Δt is $7 * 10^{-4}$ s. The gravitational force of the two masses combined is $\sum_n m_n g = 217.8N$. To make contact possible between the pantograph and the catenary, the static force is set to $F_0 = 260N$

The length of the small scale system was chosen to be as long as the spatial periodicity of the catenary, which is one span of 60 m. With the same spatial grid size there are only 302 variables for the catenary. Figure 5 compares the large-scale system simulation results at an arbitrarily chosen time to those from the small scale (SS) system proposed in this paper. A good fit of the catenary dynamics for the SS system is seen. The result from the large scale system in Fig. 5 is just a cut-out of Fig. 4 and overlayed in such a way, that it is consistent with the moving coordinates, whereas the small scale system is fully displayed.

In Figure 6 the pantograph-head displacement for both systems is depicted. It can be seen, that the SS system approach delivers a good approximation of the coupled pantograph and catenary dynamics.

Figure 7 shows the power spectral density for the pantograph-head-displacement. The peak for both systems at around 10 Hz is the result from the static displacement of the contact wire due to the droppers.

4.3 Test case 2: high constant force F_0

The parameters, spatial grid size and temporal grid size where chosen as in the first test case, but the constant force F_0 was set to 460 N. A comparison between the large and the small system can be seen in Fig. 8. A higher constant force F_0 tends to increase the difference between the two systems. This can also be seen by comparing the

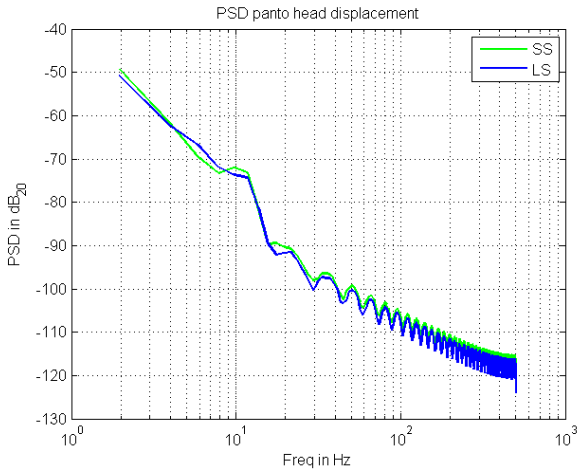

Fig. 7. Power spectral density for the pantograph-head-displacement with $F_0 = 260$ N

pantograph-head-displacement in Fig. 9. One reason for this is that in the LS system slackening of droppers is considered whereas in the SS system it is not because of the decoupled computation of the static and dynamic solution. Still, the SS system approximates the general dynamics of the catenary and pantograph well, while greatly reducing the computation time, which can be seen in the runtime comparison below.

4.4 Runtime comparison

With the speed of the pantograph chosen as in the examples above, it takes 0.864 s for the pantograph to pass one span of the catenary. The minimum length of the LS system has to be adjusted accordingly for a desired simulation time. A further increase of the LS is necessary so that the unphysical reflections at the boundary do not reach and disturb the pantograph. The length of the SS system is, as mentioned before, independent from the simulation time. The mean runtime for one time step for the LS system is continuously increasing with the simulation time (number of spans) while the runtime of the SS system is not affected by increasing the simulation time.

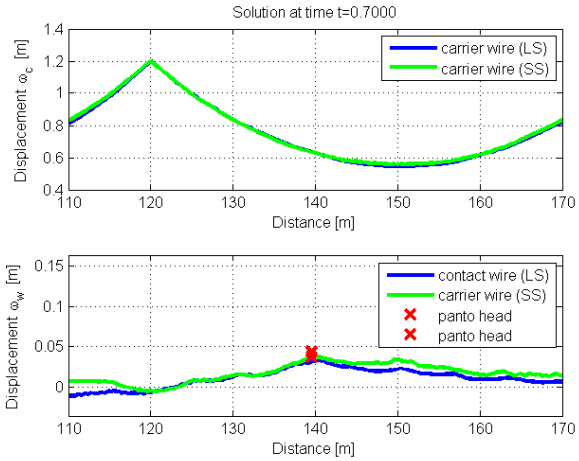

Fig. 8. Comparison between large scale (blue) and small scale (green) system with $F_0 = 460$ N. Node spacing Δx= 0.4 m

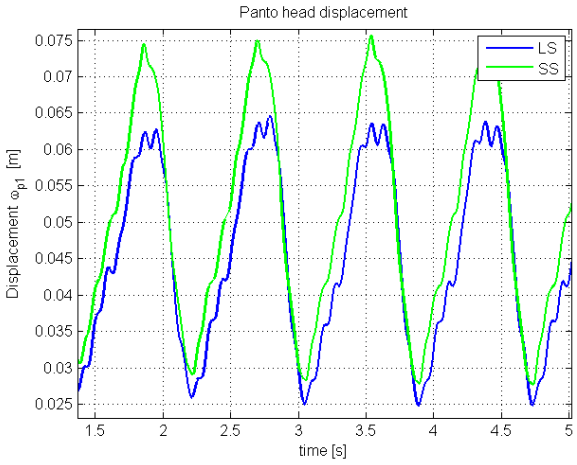

Fig. 9. Displacement over time for the pantograph head for the large scale (blue) and small scale (green) system with $F_0 = 460$ N

In the previous test cases, both systems (LS and SS) were set to a simulation time span of 10s. The runtime for the LS system was 90.1s, whereas the runtime for the SS system was 14.9s. The computations were done on a personal laptop computer (i7-4702MQ @ 2.20Ghz CPU, 8GB RAM). The new formulation proposed in this paper reduced the computation time close to a real-time computation.

5. CONCLUSION

In this paper, a new system formulation for the coupled catenary/ pantograph dynamics was proposed. The investigated test cases showed, that the new small scale system, gives a good approximation of a non-moving large scale system with far less variables that have to be computed each time step. Reducing the number of variables led to a faster computation time for each time step. Furthermore, the maximum simulation time is now independent from the size of the discrete system. The ability to arbitrarily chose the simulation time without changing the discrete system,

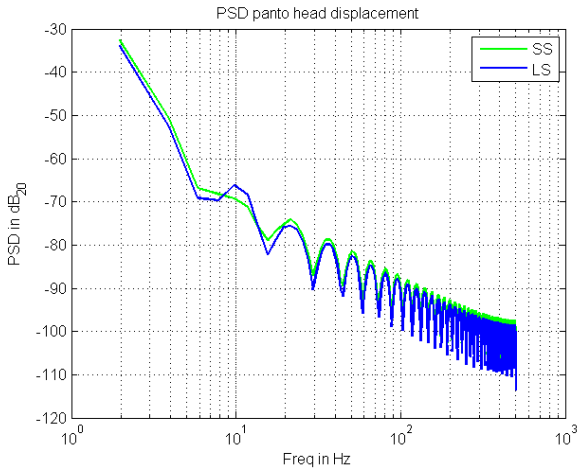

Fig. 10. Power spectral density for the pantograph-head-displacement with $F_0 = 460$ [N]

and the fast computation time makes this approach suitable for real-time applications.

REFERENCES

Arnold, M. and Simeon, B. (2000). Pantograph and catenary dynamics: a benchmark problem and its numerical solution. *Applied Numerical Mathematics*, 34(4), 345–362.

Engquist, B. and Majda, A. (1977). Absorbing boundary conditions for numerical simulation of waves. *Proceedings of the National Academy of Sciences*, 74(5), 1765–1766.

Facchinetti, A. and Bruni, S. (2012). Hardware-in-the-loop hybrid simulation of pantograph–catenary interaction. *Journal of Sound and Vibration*, 331(12), 2783–2797.

Gustafsson, B., Kreiss, H.O., and Oliger, J. (2013). *Time-dependent problems and difference methods*, volume 121. John Wiley & Sons.

Higdon, R.L. (1987). Numerical absorbing boundary conditions for the wave equation. *Mathematics of computation*, 49(179), 65–90.

Poetsch, G., Evans, J., Meisinger, R., Kortüm, W., Baldauf, W., Veitl, A., and Wallaschek, J. (1997). Pantograph/catenary dynamics and control. *Vehicle System Dynamics*, 28(2-3), 159–195.

Pombo, J., Ambrósio, J., Pereira, M., Rauter, F., Collina, A., and Facchinetti, A. (2009). Influence of the aerodynamic forces on the pantograph–catenary system for high-speed trains. *Vehicle System Dynamics*, 47(11), 1327–1347.

Schirrer, A., Talic, E., Aschauer, G., Kozek, M., and Jakubek, S. (2014). Determination of highly absorbing boundary conditions for linear finite difference schemes by multi-objective optimization. *Computational Physics*. Submitted, under review.

Zhang, W., Mei, G., Wu, X., and Shen, Z. (2002). Hybrid simulation of dynamics for the pantograph-catenary system. *Vehicle System Dynamics*, 38(6), 393–414.